CHAPTER II

DEVELOPMENT OF FLEXIBLE AND ROBUST WEARABLE ANTENNA

2.1   Introduction

2.2   Technique used for enhancing adhesion

2.3   Fabrication of the copper laminated silicone rubber-foam substrate

      2.3.1 Adhesion of silicone rubber and foam

      2.3.2 Adhesion of silicone foam substrate to metal layer

2.4   Material characterization of the fabricated silicone-foam substrate

      2.4.1 Tensile and adhesive strength test

      2.4.2 Thermo-gravimetric analysis (TGA)

      2.4.3 Water absorbance test

2.5   Microwave characterization of silicone-foam substrate

2.6   Realization of wearable antenna on silicone-foam substrate

      2.6.1 Antenna characterization techniques

      2.6.2 Performance study of antenna in flat profile

      2.6.3 Performance study of antenna for different bending profiles

2.7   Summary

      References

2.1   INTRODUCTION

A traditional patch antenna consists of a non-conducting substrate and conducting patch and ground plane. Developing a flexible antenna, in essence, would require the conducting and the non-conducting (dielectric) materials to be flexible enough and adhered strongly to each other so as to withstand the bending cycles [1].

Polymers, generally are low permittivity flexible materials with low loss, are non-reactive, stable, and resistant to environmental changes and hence considered suitable for antenna substrates. PDMS, PET, Kapton, LLDPE are some of the polymers as listed in Section 1.1 of Chapter I that have been used as substrates for flexible antenna. Amongst such polymers, silicone rubber [2, 3, 4] have the advantage of being able to be moulded and cured at the room temperature making the fabrication process easier and hence it has been considered as the substrate material in the current work. Apart from the substrate, as discussed in Chapter I, the conductivity of the patch and ground plane layers are crucial in attaining sufficient gain and efficiency values for an antenna. Copper being highly conductive ($\sigma \sim 10^7$ S/m), thin copper sheets which possesses sufficient flexibility can be a good candidate for employing as conducting layers of a flexible antenna [5, 6]. Herein, a commercial copper metal-based tape of thickness 0.03mm (>> skin depth ~ 0.65 µm at 10 GHz) has been used as the conducting material for the study.

Silicone rubber alike other polymers has low surface energy and do not adhere strongly with metals [7] which poses a major hindrance in its use as substrate. The current study addresses the issue and an effort is made to improve the adhesion between silicone and copper. The proposed 'modified' substrate is tested for use in the development of a flexible microstrip patch antenna in this work. Before moulding the material as the substrate for microstrip patch antenna (MPA), its physical and thermal properties, relevant to the application as flexible antenna substrate such as tensile strength, peel strength, and water absorbance have been studied. Complex permittivity of the substrate is measured in the

range 8.2-12.4 GHz. A simple rectangular patch antenna is then designed on the substrate using a transmission line model (TLM) technique at 10 GHz, and antenna performance is tested with different bending radii.

2.2   TECHNIQUE USED FOR ENHANCING ADHESION

Adhesion between two surfaces, generally, results from any one or more than one of the phenomena viz. Van der Waals interactions, diffusion, chemical interactions, and mechanical interlocking. Van der Waals interactions are insufficient for adhering the metal to silicone rubber as the latter is known to have very low surface energies [8]. Silicone rubber is insoluble in all but perfluorinated solvents and materials, thus diffusive adhesion is also excluded [9]. The chemical inertness of silicone rubber reduces the provision of adhesion mechanisms due to chemical interactions [8]. Mechanical interlocking is a process inspired by the "Velcro" mechanical interlocking approach, wherein an adhesion facilitator is used to improve the adhesion between two low surface energy substrates, for e.g., Zinc Oxide (ZnO) nanoparticles were used as adhesion facilitators to adhere polytetrafluoroethylene (PTFE) substrates [10].

A simpler and inexpensive concept based on "Velcro" mechanical interlocking is presented in the current study, wherein a foam layer is used as an adhesion facilitator to adhere the metal (copper) layers with silicone. Also, foam is quite flexible and has an effective permittivity close to that of the air, exhibiting low losses in the microwave regime and does not affect the properties of the composite substrate adversely.

2.3   FABRICATION OF THE COPPER LAMINATED SILICONE RUBBER-FOAM SUBSTRATE

The process of fabrication of the copper laminated silicone-foam substrate is realized in two stages. Initially, silicone rubber and foam layer are attached to obtain a silicone-foam substrate and in the subsequent stage copper layers are adhered to the silicone-foam substrate.
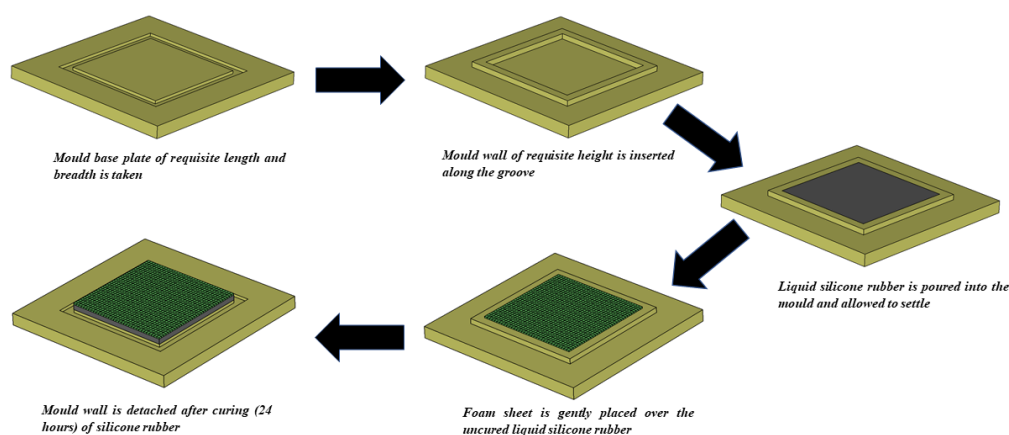
2.3.1 Adhesion of Silicone Rubber and Foam

The adhesion of silicone to foam is carried out in a two-step process. In the first step, uncured silicone rubber (purchased from MoldSil, India) is mixed with 5 wt. % hardener (purchased from MoldSil, India) and mixed thoroughly in a glass container. The mixture is then poured gently into a 3D printer (Boxzy, USA) printed Polylactic Acid (PLA) mould of dimension 50mm x 50mm x 0.75 mm. The mixture is very slowly poured so as to avoid the formation of any air bubbles until it fills up to the height of the mould. Once the uncured silicone rubber settles, in the second step, a low-density polyurethane foam sheet (density – 8.54 kg/m³) of dimension 50mm x 50mm x 3mm (length x breadth x height) is gently placed over the uncured silicone rubber. Open-cell type foam is chosen, so that the foam's cells act as air pockets allowing the uncured liquid silicone rubber to rise along these pockets. The air pockets in the foam sheet act as the capillaries and the silicone rubber is the liquid in question. As the foam sheet is placed over the uncured silicone rubber, the silicone liquid rises along the foam air pockets due to surface tension. This rise (height) is governed by the general capillary rise relation given by Equation (2.1)

$$h = \frac{2T\cos\theta}{\rho g r} \qquad (2.1)$$

wherein, T is the surface tension of the silicone rubber, θ, is the contact angle between silicone rubber and foam sheet, ρ is the density of the silicone rubber, g is acceleration due to gravity and r is the radius of the air pockets of the foam sheet. In the current case, the surface tension, T, of silicone is a function of its state, that changes with time and temperature. T decreases as the silicone hardens and further penetration is stalled. Thus, a trade-off needs to be attained for the silicone to get rooted inside sufficiently to achieve the required interlocking between the foam sheet and the silicone layer and at the same time avoid deeper penetration to sustain the structure of the substrate. MoldSil silicone rubber hardens completely in a time span of 24 hours at room temperature. Considering this fact, several rounds of trials were carried out and it was found that, if the

initial curing process (i.e., the first hour after mixing the liquid silicone with hardener) is carried out at a higher temperature of about 60°C, it fastens the process of curing and hardens the silicone to stall further penetration into the foam layer and giving sufficient bonding with the silicone surface. The remaining curing process can be carried out at room temperature conditions. The schematic of the process explained above is shown in Figure 2.1.

Mould base plate of requisite length and breadth is taken

Mould wall of requisite height is inserted along the groove

Liquid silicone rubber is poured into the mould and allowed to settle

Mould wall is detached after curing (24 hours) of silicone rubber

*Foam sheet is gently placed over the uncured liquid silicone rubber*

Figure 2.1 Schematic of the workflow for the synthesis of the silicone-foam substrate (Colour code of the layers: Grey – silicone rubber; Green - foam)
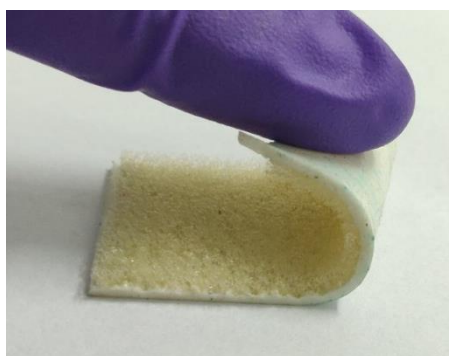
Figure 2.2 Synthesized silicone-foam substrate

Once the silicone rubber gets cured in about 24 hours, it gets well rooted into the foam sheet as shown in Figure 2.2. This phenomenon is quite evident if the foam sheet is removed by force the top layer of the silicone appears to contain micro spikes which were formed due to the capillary rise of silicone rubber inside the foam sheet cells. A photograph of the silicone layer as it appears to be after the foam sheet is detached is shown in Figure 2.3(a). A magnified image of a region

of the layer is taken using the foldscope [10] and is shown in Figure 2.3(b). The sample is kept on a glass slide which is attached to the foldscope and the image is taken using a mobile phone camera. In order to brighten the image, the slide is lighted from its rear using a led flashlight. Therefore, the silicone spikes appear dark in the image as shown in Figure 2.3(b).


(a)   *(b)*
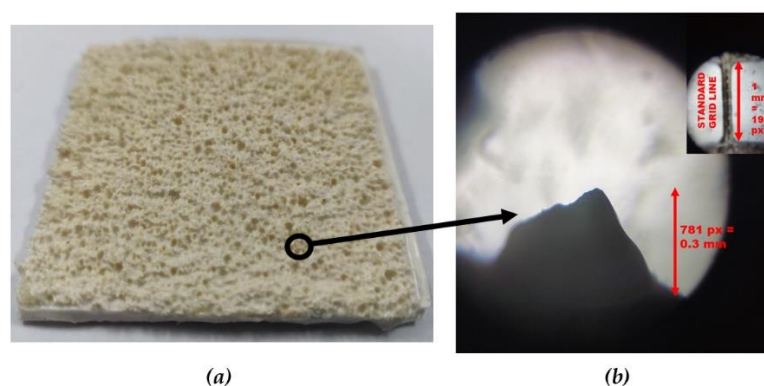
Figure 2.3 (a) Photograph illustrating the spikes on silicone surface exposed after removing the foam sheet by force from the silicone-foam substrate and (b) a magnified image of one of such spikes using a foldscope

The height of the spike as seen from the image is estimated using a standard grid line image taken by the same foldscope. The height of this spike is found to be 0.3 mm.

2.3.2 Adhesion of silicone foam substrate to metal layer

The second step of the fabrication process is copper lamination. A thin copper sheet of dimension 50mm x 50mm x 0.03 mm is prepared by scrubbing and cleaning its surface with ethanol and then dried in a hot air oven at 60°C for 60 minutes. The foam surface of the silicone-foam substrate, fabricated in the above process, is cleaned by blowing dry air. A polyurethane-based binder (PU-binder) is chosen for binding the copper sheet and the silicone-foam substrate. The binder is uniformly applied on the foam side of the silicone-foam substrate until it completely percolates the foam layer and then on the copper sheet. The surfaces are then left to dry at room temperature for about 5 minutes so that the solvent of the binder evaporates. The smeared copper sheet is then placed on the substrate and pressed uniformly in a standard table vice for about 12 hours to get

a sufficiently strong adhesion. The obtained copper laminated silicone-foam substrate is shown in Figure 2.5.
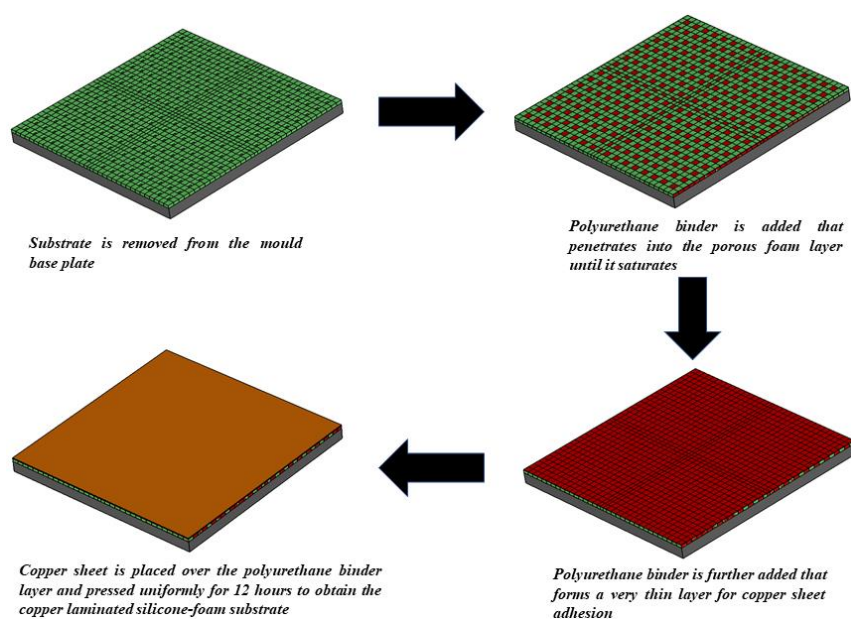
Figure 2.4 Schematic of the workflow for adhering the copper sheet to the silicone-foam substrate using PU-binder (Colour code of the layers: Grey – silicone rubber; Green – foam; Red – PU binder; Brown – copper sheet)
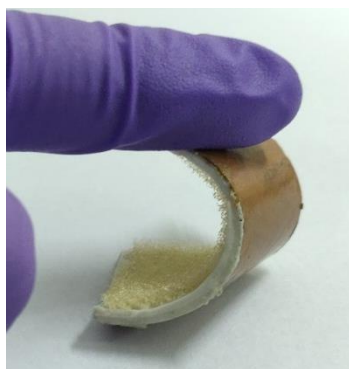
Figure 2.5 Silicone-foam substrate adhered to a metal sheet using a PU-binder on one side

Since for an antenna, metallic layers are required on both top and bottom of the substrate the above mentioned two processes, are repeated in the same manner to obtain another set of the silicone-foam copper multi-layered substrate with the same dimension 50mm x 50mm x 0.75mm (length x breadth x thickness). The obtained pair of substrates are then bonded together by applying a very thin layer of silicone (mixed with hardener) over the silicone side of the substrates

and then placed over one another. The structure is left to dry at room temperature for 24 hours.

2.4 MATERIAL CHARACTERIZATION OF THE FABRICATED SILICONE-FOAM SUBSTRATE

The physical properties such as tensile strength, adhesive (peel) strength, thermal stability, water absorbance of the developed substrate is tested to determine its usability as an antenna substrate.

2.4.1 Tensile and adhesive strength test

A silicone-foam-binder substrate (without copper lamination) and a pure silicone substrate (without the foam and copper lamination) is subjected to a tensile strength test. for determining its flexibility and stretchability using Universal Testing Machine (UTM); Make – Zwick; Model – Roel 10kN; Testing Standard – ASTM D 882 at room temperature with a 500 N load cell and a crosshead speed of 20 mm/min. The schematic of the measurement is shown in the inset of Figure 2.6.
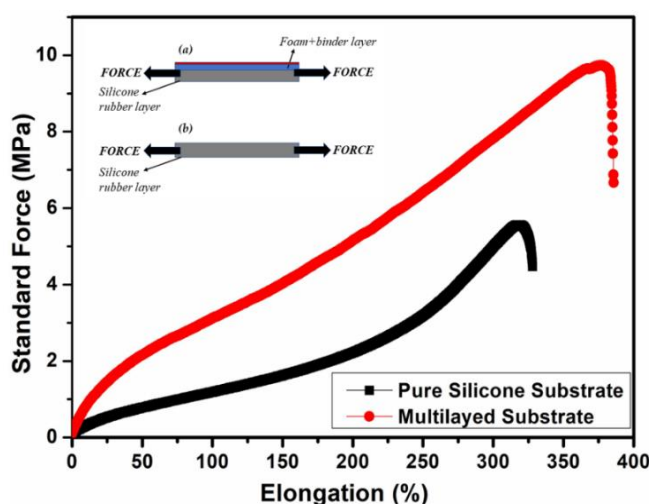

Figure 2.6 Tensile strength of pure silicone and developed multi-layered substrate. Inset - schematic of the test set up for (a) silicone-foam-PU binder multi-layered substrate and (b) only silicone substrate

From Figure 2.6 it is seen that the elongation at break for the multi-layered silicone-foam substrate is higher at around 375% compared to pure silicone at

around 325%. The increased elongation at break for the multi-layered substrate could be due to the interlocking of silicone in the pockets of foam (Figure 2.3).

The adhesion strength (peel strength) of copper to the foam-silicone substrate via the PU binder is also tested using UTM. The schematic set up for measuring the peel strength is as shown in the inset of Figure 2.7. Two similar sets of the multilayer substrates are adhered together through a copper sheet layer having a surface contact area of 4 cm². The substrates are then subjected to a standard force and the corresponding elongation is measured until the copper sheet is peeled off from any of the two substrates.
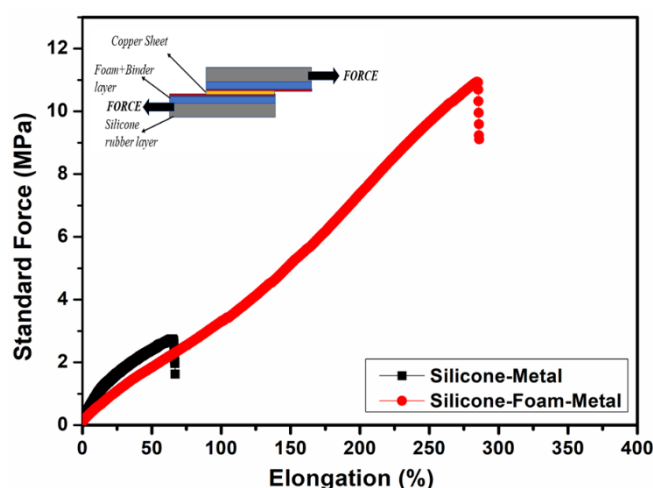

Figure 2.7 Adhesive (peel) strength of copper to multi-layered substrate vide PU-binder (red) and copper to silicone vide cyanoacrylate binder (black). Inset - schematic of the test set up for adhesive (peel) strength test

The multi-layered substrate with copper sheet attachment vide PU binder shows an elongation of up to around 275% (marked as silicone-foam-metal in Figure 2.7) which is about three times of the original substrate length before the copper sheet peeled off completely. It is noteworthy to mention here that the silicone does not stick to metal vide PU binder directly (because of low surface energies). On adhering copper sheet directly to silicone via another common binder based on cyanoacrylate exhibits an elongation of 75% (marked as silicone-metal) as shown in Figure 2.7. Foam could not be used as an adhesion facilitator in this case, as cyanoacrylate dissolves the foam as soon as it comes in contact with it.

The results of the adhesive strength characterizations, indicate that the developed silicone-foam substrate's adherence to the metallic layer is sufficiently high [10], so that the layer does not tend to come off due to bending and thus, the foam layer in the silicone-foam substrate acts as an adhesion enhancer for silicone to copper adhesion.

2.4.2   Thermo-Gravimetric Analysis (TGA)

The thermo-gravimetric analysis (TGA) of the fabricated silicone-foam-binder (without copper lamination) substrate is carried out using a thermogravimetric analyzer, model STA-6000. 14 mg piece of the sample is heated at a rate of 10°C/min in the temperature range of 15–600°C under a constant nitrogen atmosphere to determine the decomposition temperatures.
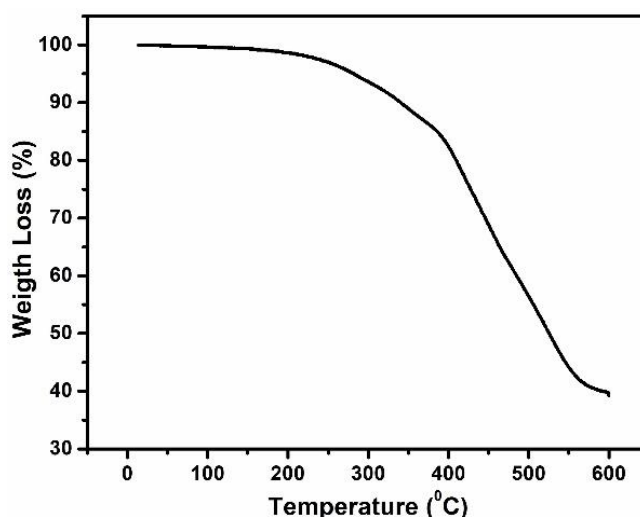
Figure 2.8 TGA curve of the multi-layered substrate

As evident from the Figure 2.8, the structure exhibits a mass loss of 1% up to 180°C, beyond which the rate of degradation increases. The major weight losses take place at around 200°C and 400°C because of the decomposition of foam [11] and PU-binder [12], silicone rubber [13] respectively.

2.4.3   Water absorbance test

The developed multilayer silicone-foam-binder substrate is submerged in distilled water at room temperature condition for around 72 hours and their

respective weights are recorded before submerging and after submerging to determine the percentage of water absorbance of the substrates under study. The water absorbance test reveals that there is no change in the weight up to an accuracy of 0.001 gm, for silicone-foam-binder substrate, after submerging it in water for a period of 72 hours. The result is quite evident, because of the fact that silicone is known to have a water repellent property and is commonly used in industries as sealants and moisture protective sheets. The PU binder layer is also water repelling in nature, however, the foam does absorb water. The PU binder and the silicone that penetrates inside the air pockets of the foam layer alienates the possibility of water seepage into the multi-layered substrate.

2.5 MICROWAVE CHARACTERIZATION OF THE SILICONE-FOAM SUBSTRATE

The microwave characterization of the multi-layered substrate i.e., silicone attached to foam on both its top and bottom surfaces along with the PU binder applied over the foam surface are measured using Agilent WR-90 X11644A rectangular waveguide line compatible to Agilent E8362C VNA with sample size 22.86mm x 10.16mm. The complex permittivity ($\varepsilon_r = \varepsilon_r' - \varepsilon_r''$) in the X-band frequency range (8.2-12.4 GHz) are computed using Agilent 85071E material measurement software employing Nicolson Ross Weir technique [14, 15]. The measurement set up is shown in Figure 2.9.
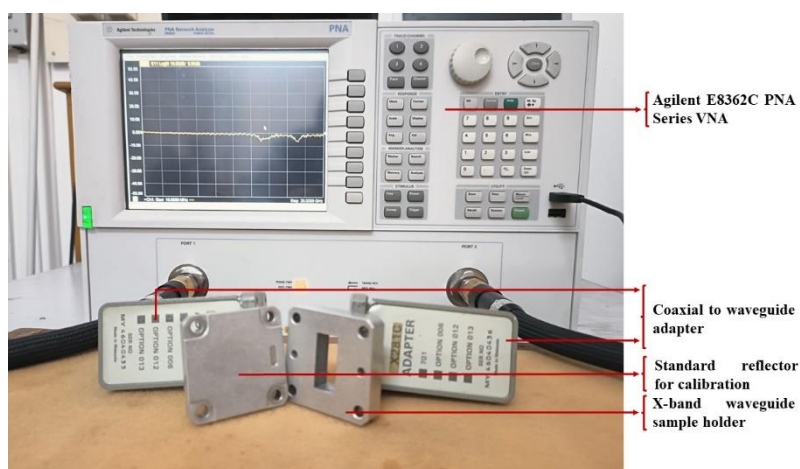
Figure 2.9 Photograph of the Agilent WR-90 X11644A rectangular waveguide line with Agilent E8362C VNA

The components of the multi-layered substrate vide the silicone, foam-binder (the PU-binder penetrates the foam as it is spread on it and thus has been considered as a distinct layer) and binder are also individually characterized for their dielectric properties. Figure 2.10 shows the permittivity (ε_r') and loss tangent ($tan\delta = \varepsilon_r''/\varepsilon_r'$) of the individual layer materials that make up the multi-layered silicone-foam substrate. The measurements are taken over the X-band range as the substrate is intended to be used in an antenna working in the said frequency regime.
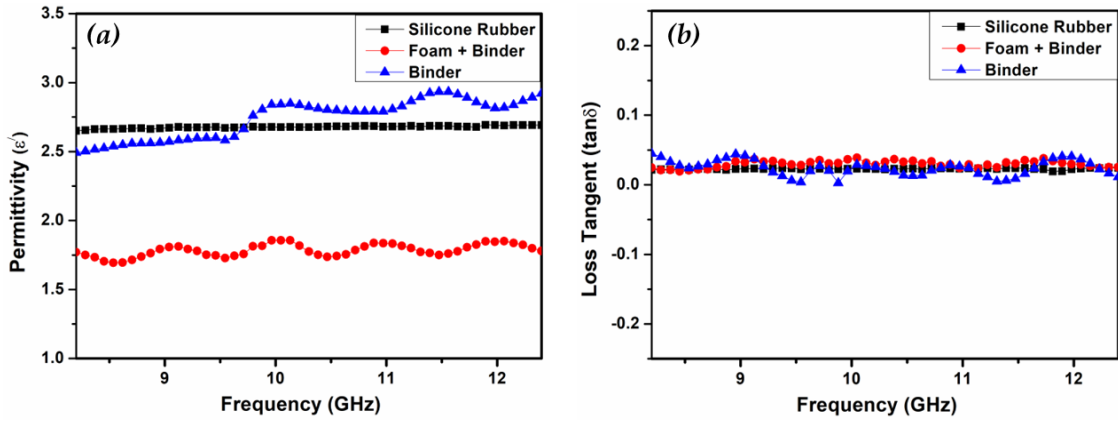

Figure 2.10 (a) Permittivity of individual layers comprising the multi-layered substrate and (b) loss tangent of individual layers comprising the multi-layered substrate

The measured values of the individual layer materials are used for obtaining the calculated permittivity values of the multi-layered substrate and the multi-layered substrate is characterized to obtain the measured values as well. The calculated dielectric permittivity for the three-layer substrate is obtained using the Equation (2.2) [16, 17] as shown below,

$$\epsilon_{rc} = \frac{\sum_{i=1}^{3} h_i}{\sum_{i=1}^{3} \frac{h_i}{\epsilon_i}} \qquad (2.2)$$

wherein, ϵ_i and h_i are the dielectric permittivity and height of the individual component layers of the multi-layered substrate respectively. The individual permittivity values are obtained from the measured permittivity curves. The height of the individual layers is measured and accordingly put in Equation (2.2), to obtain the calculated values. Here the thickness of the individual layer is kept

the same as the actual dimensions. The measured and calculated permittivity plots are shown in Figure 2.11(a) and are in good agreement with each other. Figure 2.11(b) shows the measured permittivity and loss tangent plots of the silicone-foam multi-layered substrate.
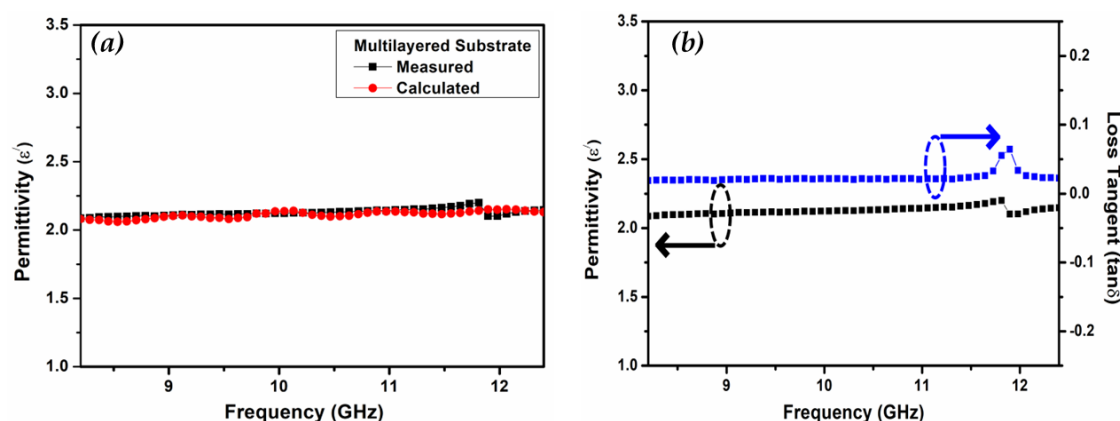
Figure 2.11 (a) Comparison of calculated and measured permittivity of multi-layered substrate and (b) measured permittivity and loss tangent of the multi-layered substrate

The permittivity and the loss tangent values of the silicone-foam substrate in the frequency range 8.2-12.4 GHz vary in the range 2.08 to 2.20 and 0.01 to 0.06 respectively. The dielectric characteristics also show that the substrate has low permittivity and low loss in the X-band frequency range indicating that the gain of the antenna would not be adversely affected [18].

2.6 REALIZATION OF A WEARABLE ANTENNA ON THE SILICONE-FOAM SUBSTRATE

A simple microstrip patch antenna is designed on the developed substrate to resonate at 10 GHz, considering the dielectric constant at 10 GHz to be 2.12, loss tangent to be 0.02 (as obtained from Figure 2.11) and the substrate thickness to be 2 mm. The standard transmission line model [19] is employed to determine the patch size. The obtained patch dimensions are then used to model a simple microstrip patch antenna using CST Microwave Studio simulation software and optimized to resonate at 10 GHz using time domain solver and an in-built optimizer. The schematic of the modelled patch, as well as the cross-section of the

modelled substrate, are shown in Figure 2.12 and the optimized dimensions are tabulated in Table 2.1. The S_{11} curve of the modelled antenna and the radiation pattern at the corresponding resonant frequency is plotted in Figure 2.16 and 2.18 respectively.

Table 2.1 CST configuration for patch dimension optimization

CST Configuration	Optimization Target	Optimized parameters (in mm)						
		c	*d*	*e*	*f*	*g*	*h*	*i*
Time Domain Solver Trust Region Framework Algorithm	**Resonant Frequency ~ 9.99-10.01 GHz**	10.16	12.00	18.00	1.85	3.08	6.30	1.0
	$S_{11} < -20\ dB$							
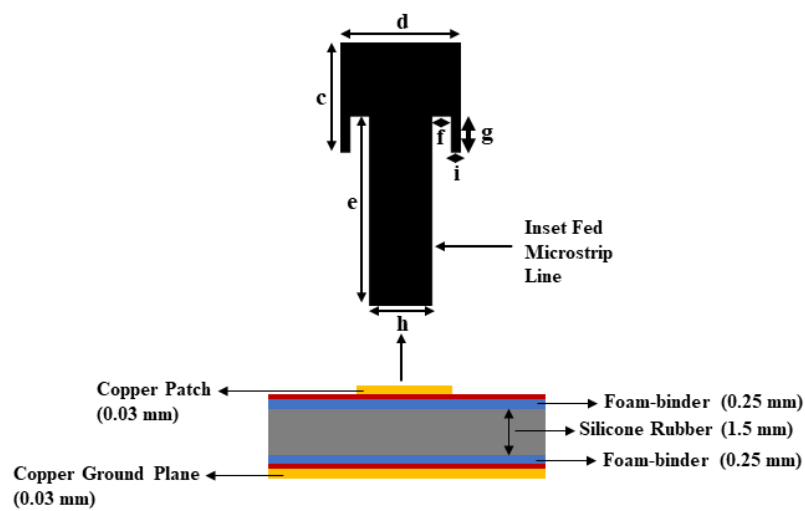
Figure 2.12 Schematic of patch dimensions of the designed microstrip patch antenna (top) and cross-section of the designed microstrip patch antenna (bottom)

This simulated antenna structure is then fabricated for experimental verification. The copper laminated (top + bottom) silicone-foam substrate is obtained by following the procedure described in the previous section. One side of the copper lamination is cleaned thoroughly by using ethanol and washed with water several times to remove traces of the chemical before drying it in a hot air oven at 60°C for 30 mins. The patch design artwork is printed on a plain photo paper sheet and the artwork is transferred onto the cleaned side of the copper lamination by hot press technique. The other copper laminated side is masked by tape. The structure is dipped into a solution of ferric chloride and the solution is

stirred slowly until the desired patch design is completely etched. The photographs of the fabricated antenna are shown in Figure 2.13.
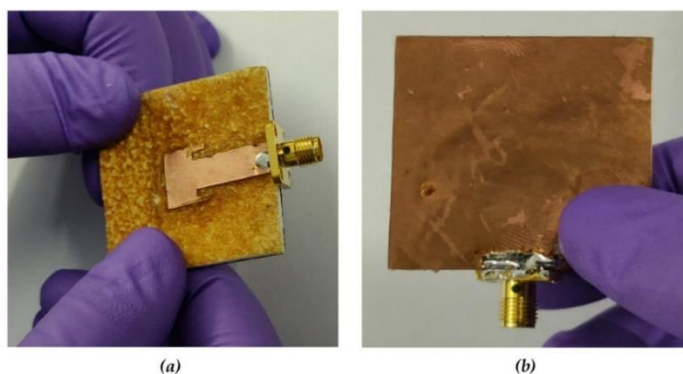

Figure 2.13 (a) Patch view of the fabricated antenna and (b) ground plane view of the fabricated antenna

2.6.1 Antenna characterization techniques

S_{11} measurement

The measurement of S_{11} of the antennas in the current study is carried out using Agilent E8362C PNA series Vector Network Analyzer (VNA). Calibration is done prior to measurements using Agilent 85052D calibration kit vide a short, open, and broadband load as shown in Figure 2.14.
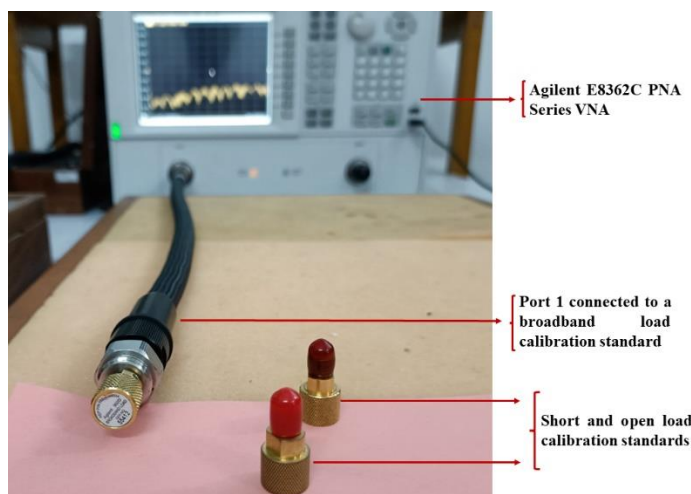
Figure 2.14 Photograph of the Agilent E8362C PNA series VNA with Agilent 85052 calibration standards

The antenna under test (AUT) in connected to the port 1 of the VNA and the frequency is swept from 8.2 to 12.4 GHz with a resolution of 0.21 MHz.

Radiation pattern measurement

The radiation pattern measurement is carried out using an automated antenna measurement system from Diamond Engineering, USA, model DAMS 6000 series turn table with an attachable mount for full spherical measurements with 2.3 kg load capacity. The system has a resolution of 0.06° over both azimuth and elevation. The set-up is shown in Figure 2.15.

**Figure 2.15** Photograph of the automated antenna measurement system from Diamond Engineering, USA (Model – DAMS 6000 with FSM)

The AUT is connected through the spherical mount/turn table to the port-2 of the VNA and port 1 is connected to a standard gain horn antenna. The measured data is acquired through the GPIB interface of the VNA and fed into the Diamond Antenna Measurement Studio (DAMS) software to the extract the post processed results vide, normalized pattern, gain and directivity.

2.6.2   Performance study of antenna in flat profile

The antenna fabricated (refer to Figure 2.13) is characterized for its S_{11} to determine its resonating ability. A full wave simulation is also carried out using CST microwave studio. Both the simulated and measured plots are shown in Figure 2.16.
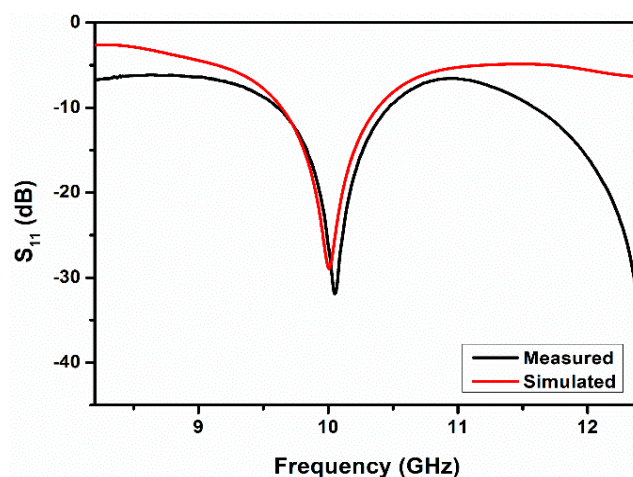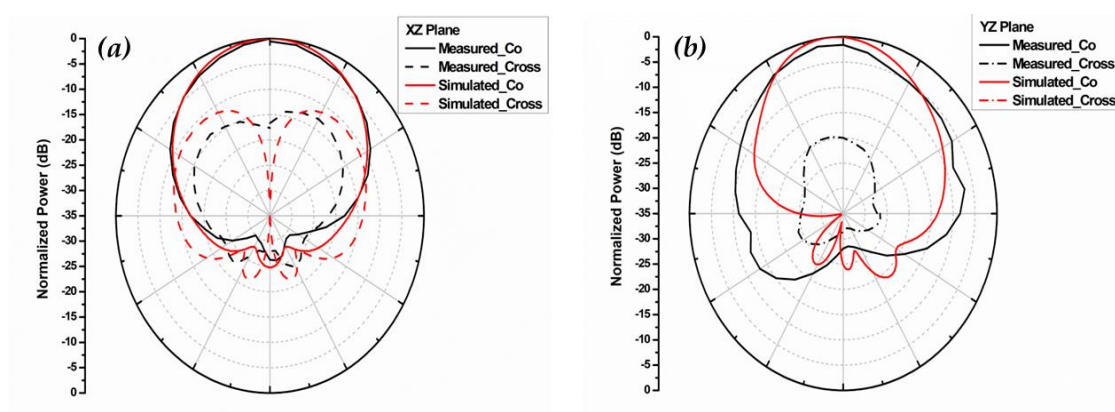
Figure 2.16 Simulated and measured S_{11} of the fabricated antenna in flat profile

The radiation measurements are carried out along two orthogonal broadside planes XZ and YZ as shown in the Figure 2.17 and the results are plotted in Figure 2.18.
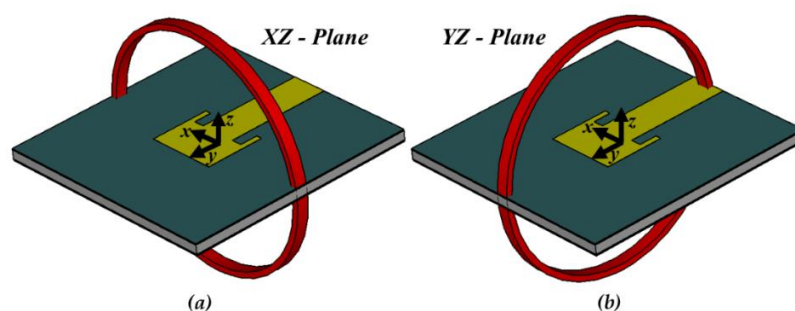
Figure 2.17 Broadside radiation pattern planes indicated by the red circle (a) XZ plane and (b) YZ plane, that have been considered for measurement in this study

Figure 2.18 Simulated and measured normalized radiation pattern of the antenna in a flat profile (i.e., in the unbent condition) of (a) XZ plane and (b) YZ plane

Slight deviation as observed from the simulated and measured curves may be due to fabrication tolerances and modelling limitations in the CST microwave studio owing to the cell restrictions in the version of the software used in the laboratory. Moreover, in simulation, the cross polar level of the antenna in YZ plane are much below the corresponding co-polar levels and hence the plots are not visible within the range as evident from Figure 2.18(b). A summary of the obtained results is tabulated in Table 2.2.

Table 2.2 Antenna characteristics in flat profile (unbent)

|	Resonant Frequency (GHz)	S_{11} (dB)	-10 dB % Bandwidth	Directivity (dBi)	Gain (dBi)
Measured	10.05	-31.9	8.0	12.91	7.34
Simulated	10	-28.9	7.3	9.45	7.03

As seen from Table 2.2, the antenna exhibits a measured gain of 7.34 dBi, which is high considering similar single element rectangular patch antenna on standard substrates [20].

2.6.3 Performance study of antenna for different bending profiles

As the antenna is fabricated on the flexible substrate for wearable applications, subsequent study of the effect of bending on the antenna characteristics is performed. Bending is carried by placing the antenna on three semi cylinders (3D printed PLA material) of radii 40 mm, 30 mm, and 20 mm. These radii values have been chosen keeping in view the range of radii of a healthy human arm [21]. Two bending configurations – (a) XZ bending and (b) YZ bending, as shown in the Figure 2.19, are employed for performance testing.
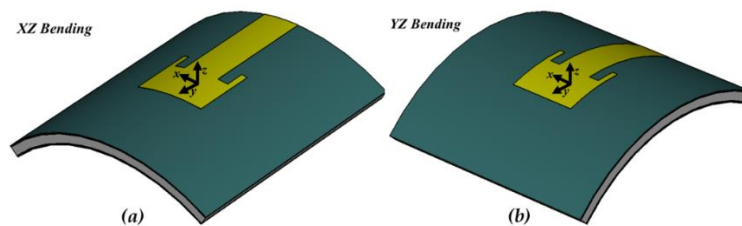

Figure 2.19 Bending profiles carried out in the current study (a) XZ bending and (b) YZ bending
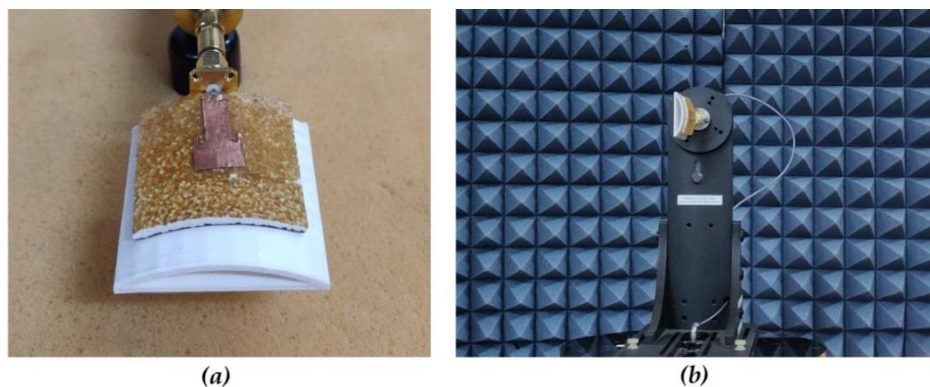
Figure 2.20 (a) Illustration of XZ bent antenna bent on a 3D printed PLA 40 mm semi-cylinder connected to one port of a VNA for S_{11} measurements and (b) illustration of antenna bent on a 40 mm 3D printed PLA semi-cylinder and mounted on a 360° turntable for radiation pattern and gain measurements

The effect on the S_{11} parameters, both measured and simulated are shown in the Figure 2.21 and Figure 2.22 respectively.
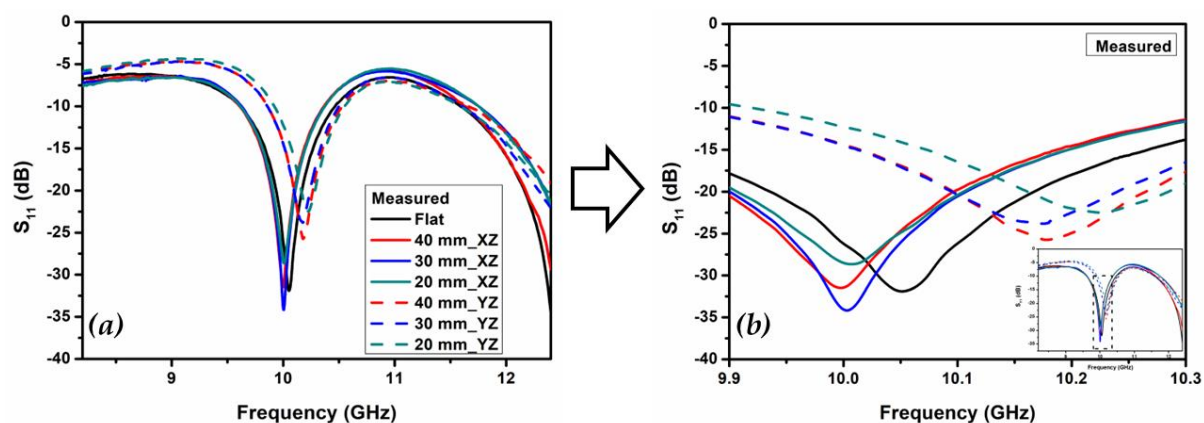
Figure 2.21 (a) Variation of S_{11} (measured) with different bending profiles and (b) a magnified image of the adjacent graph for better clarity
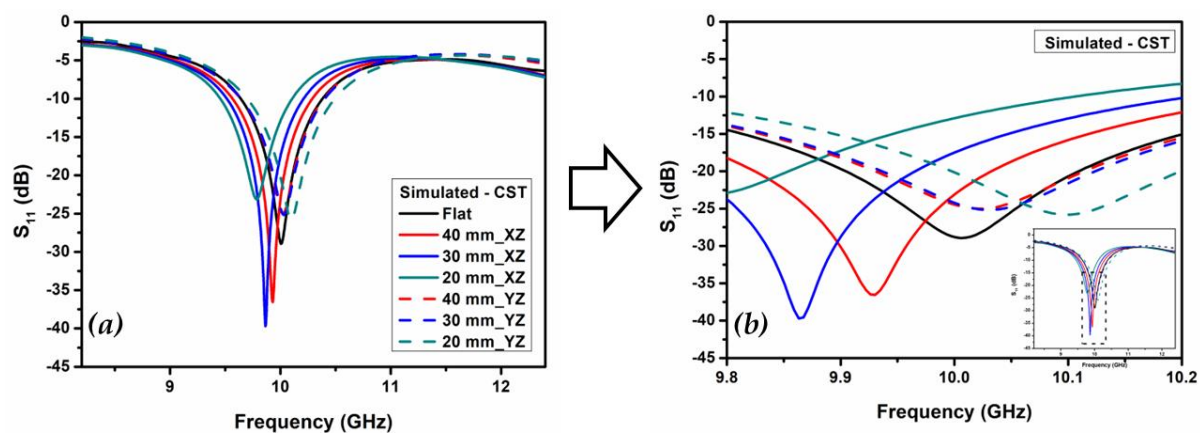
Figure 2.22 (a) Variation of S_{11} (simulated) with different bending profiles and (b) a magnified image of the adjacent graph for better clarity
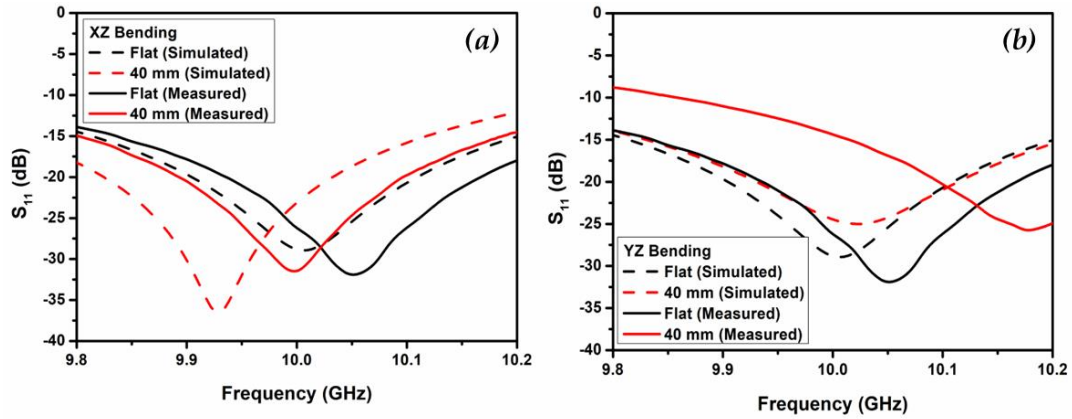
Figure 2.23 Comparison of measured and simulated results for 40 mm bending of the antenna in the (a) XZ plane (b) YZ plane

A good agreement in the trend of measured and simulated results can be clearly seen from the above plots. The trend of the shift of resonant frequency is opposite in both the cases, i.e., for XZ bending it is towards the lower frequency side while for YZ bending towards the higher frequency side. The lower frequency shift indicates an increase of electrical patch length, and the shift to higher frequency indicating a decrease in the electrical patch length. A similar trend is reported in [22] also. The -10 dB % bandwidth remains consistent with different bending configuration, with a maximum diminution of 2% for the 20mm XZ bending case. A decrease in the return loss occurs with bending, however, in all the cases it is seen that the resonant frequency notch is below -20 dB. Also, the original resonant frequency of 10.05 GHz (i.e., for the flat case) lies within the -20 dB bandwidth region for the XZ bending and within the -10 dB bandwidth region for the YZ bending.

The effect of bending on the radiation characteristics are plotted in Figure 2.23 to 2.26. The simulated and the measured results are plotted separately for better clarity. Both XZ and YZ plane measurements are carried out for XZ and YZ bending. The XZ plane radiation patterns do not undergo a change in shape, except for a broadening of the pattern in the broadside direction and increase in the back-lobe levels. In the case of YZ plane radiation patterns, the main lobe suffers a deviation, which might be due to the change in the current distribution

along the YZ plane and also due to the effect of the microstrip feed line which is lying along the YZ plane. Gain measurements were also carried out using standard gain horn antennas and have been tabulated in the summary Table 2.4.
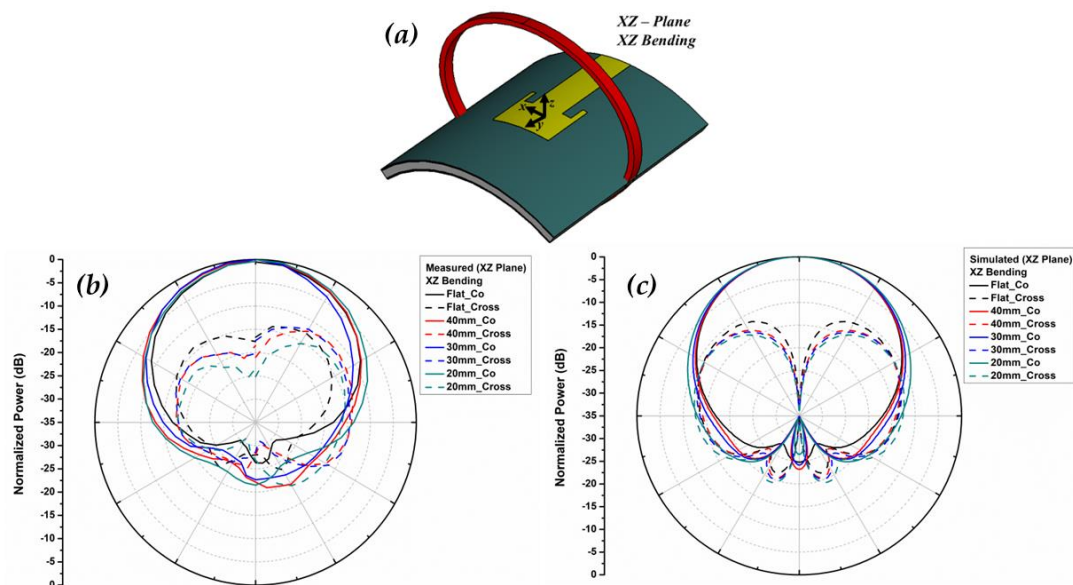
Figure 2.24 (a) Representation of the bending configuration of the antenna and the red circle representing the radiation pattern plane, (b) variation of the measured radiation pattern of the XZ plane and (c) variation of the simulated radiation pattern of the XZ plane with varying bending radii in the XZ plane
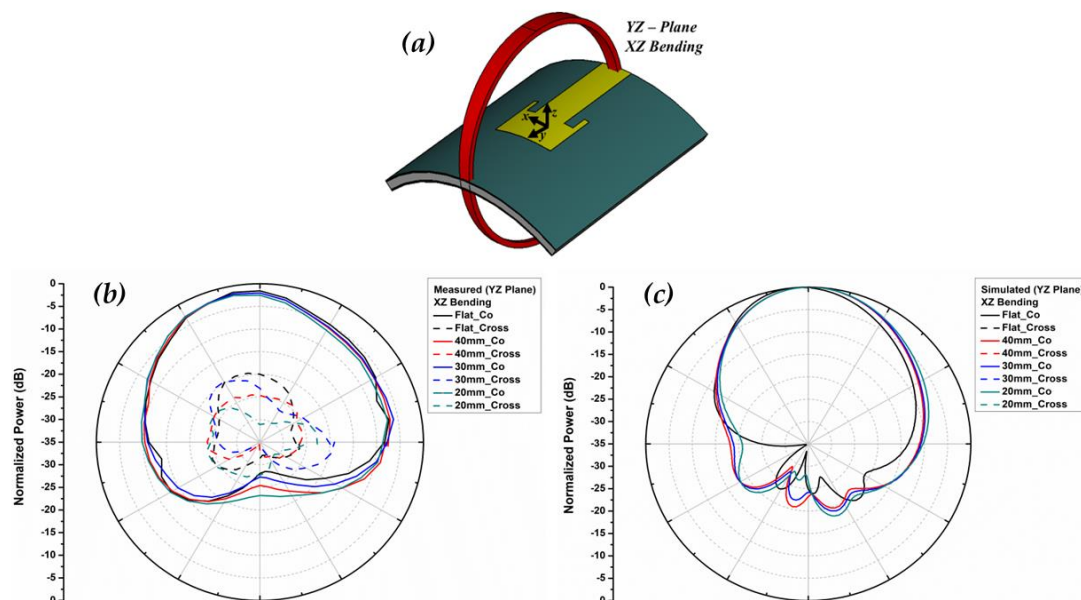
Figure 2.25 (a) Representation of the bending configuration of the antenna and the red circle representing the radiation pattern plane, (b) variation of the measured radiation pattern of the YZ plane and (c) variation of the simulated radiation pattern of the YZ plane with varying bending radii in the XZ plane.

The gain and directivity of the bent antennas are less as compared to the flat structure, although it may be noted that bent antennas still exhibit a gain of above 7 dBi.
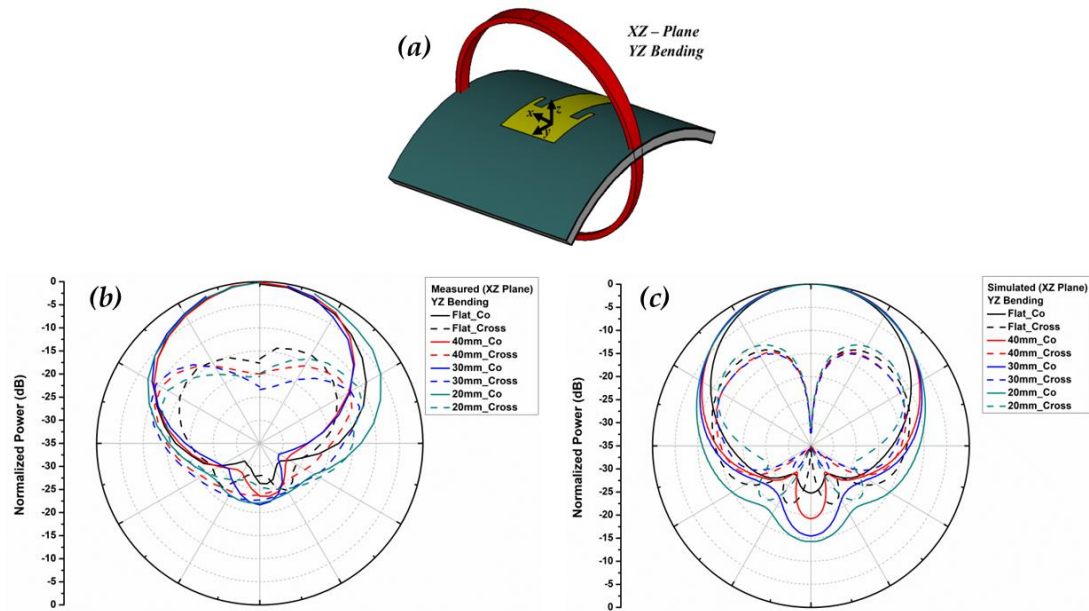

Figure 2.26 (a) Representation of the bending configuration of the antenna and the red circle representing the radiation pattern plane, (b) variation of the measured radiation pattern of the XZ plane and (c) variation of the simulated radiation pattern of the XZ plane with varying bending radii in the YZ plane
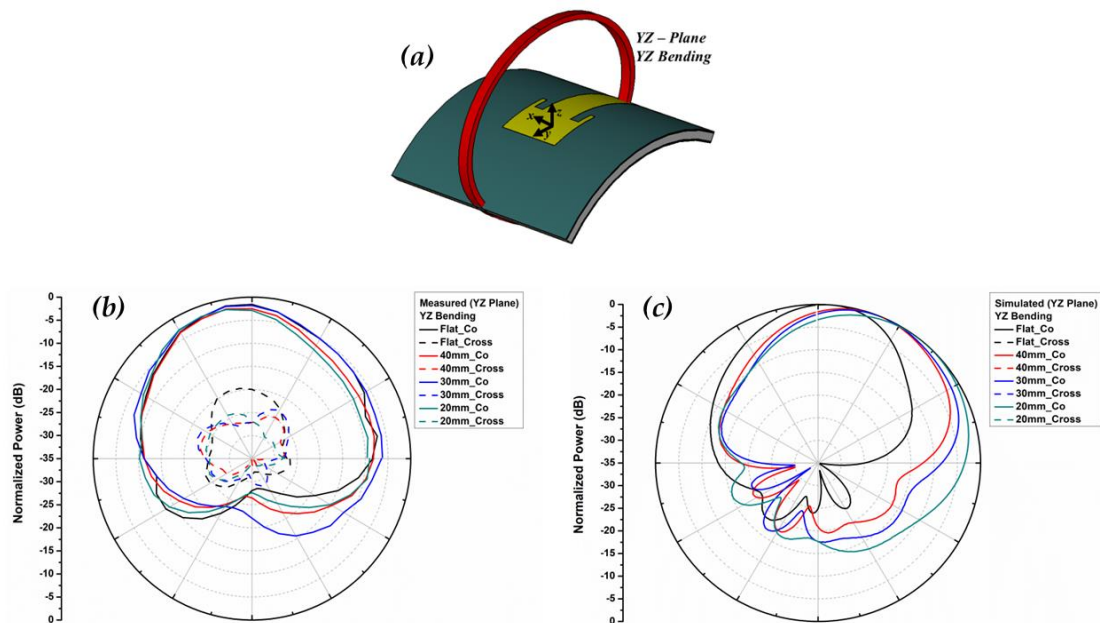

Figure 2.27 (a) Representation of the bending configuration of the antenna and the red circle representing the radiation pattern plane, (b) variation of the measured radiation pattern of the YZ plane and (c) variation of the simulated radiation pattern of the YZ plane with varying bending radii in the YZ plane

Table 2.3 Quantitative summary of the antenna characteristics in flat profile (unbent) and bent profiles

Profile	Bending Radii (mm)	Resonant Frequency (GHz)	S_{11} (dB)	-10 dB % BW	Directivity (dBi)	Gain (dBi)	Resonant Frequency (GHz)	S_{11} (dB)	-10 dB % BW	Directivity (dBi)	Gain (dBi)
					Measured					**Simulated**	
Flat	--	10.05	-31.9	8	12.9	7.9	10	-28.9	7.3	9.4	7.0
XZ bending	40	9.99	-31.4	7.1	12.7	7.7	9.93	-35.53	7.1	8.9	6.8
	30	10.00	-34.17	7.1	13.1	7.8	9.86	-39.68	7	8.7	6.6
	20	10.00	-28.65	7	12.4	7.6	9.78	-23.11	6.4	8.3	6.3
YZ bending	40	10.17	-25.74	6.2	13.0	7.5	10.03	-25.17	8	7.1	5.1
	30	10.17	-23.81	6.2	12.2	7.4	10.03	-25.17	8	8.5	6.6
	20	10.22	-22.49	5.8	12.6	7.6	10.09	-25.81	7.6	7.7	6.0

2.7   SUMMARY

An effective solution is presented to address the issue of poor adhesion of metal to silicone for the realization of flexible antennas for wearable applications. The low surface energy of silicone creates difficulties in adhering metal layers to it. Low-density polyurethane (PU) foam is used as an adhesion facilitator for interlocking silicone and a good adhesion strength with the copper layers is obtained via a commercially available polyurethane (PU) binder. The strong adhesion is verified by the peel strength test which indicates an increase in elongation by 200% for silicone-foam-metal as compared to the silicone-metal structure. The developed multi-layered substrate also illustrates a high elongation at break of around 375%, a thermal stability of upto 180°C and very low water absorbance. These physical properties warrant the robustness of the developed substrate to withstand several bending and stretching cycles as well to operate in harsh environmental conditions. The microwave characterizations show that the substrate exhibits a low permittivity value of 2.12 and a loss tangent of 0.02 at 10 GHz. The application of the substrate for wearable purpose is demonstrated by fabricating a simple microstrip antenna and testing its performance in both flat and bending profiles. The antenna characteristics exhibit a gain greater than 7 dBi. The gain and bandwidth are almost consistent for all the bending radii as well as for both the orthogonal bending planes.

References

1. Ali, E.M., Awan, W.A., Alzaidi, M.S., Alzahrani, A., Elkamchouchi, D.H., Falcone, F. and Ghoneim, S.S. A shorted stub loaded UWB flexible antenna for small IoT devices. *Sensors*, 23(2):748, 2023.

2. Awang, R.A., Baum, T., Berean, K.J., Yi, P., Kalantar-Zadeh, K., Sriram, S. and Rowe, W.S. Elastomeric composites for flexible microwave substrates. *Journal of Applied Physics*, 119(12), 2016.

3. Kaur, B., Saini, G. and Saini, A. Silicone rubber superstrate loaded patch antenna design using slotting technique. In *IOP Conference Series: Materials Science and Engineering*, Volume 149, No. 1, page 012150, September 2016, IOP Publishing.

4. Namitha, L.K. and Sebastian, M.T. Microwave dielectric properties of flexible silicone rubber–Ba (Zn1/3Ta2/3) O3 composite substrates. *Materials Research Bulletin*, 48(11):4911-4916, 2013.

5. Santas, J.G., Alomainy, A. and Hao, Y. Textile antennas for on-body communications: Techniques and properties, 2007.

6. Salonen, P., Kim, J. and Rahmat-Samii, Y. Dual-band E-shaped patch wearable textile antenna. In *2005 IEEE Antennas and Propagation Society International Symposium*, Volume 1, pages 466-469, July 2005, IEEE.

7. Paracha, K.N., Rahim, S.K.A., Soh, P.J. and Khalily, M.. Wearable antennas: A review of materials, structures, and innovative features for autonomous communication and sensing. *IEEE Access*, 7:56694-56712, 2019.

8. Jin, X., Strueben, J., Heepe, L., Kovalev, A., Mishra, Y.K., Adelung, R., Gorb, S.N. and Staubitz, A. Joining the un-joinable: adhesion between low surface energy polymers using tetrapodal ZnO linkers. *Advanced Materials*, 24(42):5676-5680, 2012.

9. Mark, J.E. Polymer Data Handbook, 2009.

10. Cybulski, J.S., Clements, J. and Prakash, M. Foldscope: origami-based paper microscope. *PloS one*, 9(6):e98781, 2014.

11. Wolska, A., Goździkiewicz, M. and Ryszkowska, J. Thermal and mechanical behaviour of flexible polyurethane foams modified with graphite and phosphorous fillers. *Journal of Materials Science*, 47:5627-5634, 2012.

12. Mamiński, M., Jaskółowski, W. and Parzuchowski, P. Thermal stability of novel polyurethane adhesives investigated by TGA. *Mediterranean Journal of Chemistry*, 3(3):877-882, 2014.

13. Gogoi, D.J. and Bhattacharyya, N.S. Embedded dielectric water "atom" array for broadband microwave absorber based on Mie resonance. *Journal of Applied Physics*, 122(17), 2017.

14. Weir, W.B. Automatic measurement of complex dielectric constant and permeability at microwave frequencies. *Proceedings of the IEEE*, 62(1):33-36, 1974.

15. Nicolson, A.M. and Ross, G.F. Measurement of the intrinsic properties of materials by time-domain techniques. *IEEE Transactions on Instrumentation and Measurement*, 19(4):377-382, 1970.

16. Jha, K.R. and Singh, G. Analysis and design of rectangular microstrip antenna on two-layer substrate materials at terahertz frequency. Journal of Computational Electronics, 9:68-78, 2010.

17. Sarmah, D., Bhattacharyya, N.S. and Bhattacharyya, S. Study of graded composite (LDPE/TiO2) materials as substrate for microstrip patch antennas in X-band. IEEE Transactions on Dielectrics and Electrical Insulation, 20(5):1845-1850, 2013.

18. Raveendran, A., Sebastian, M.T. and Raman, S. Applications of microwave materials: A review. *Journal of Electronic Materials*, 48:2601-2634, 2019.

19. Balanis, C.A. *Antenna theory: analysis and design*. John Wiley & Sons, 2016.

20. Rabbani, M.S. and Ghafouri-Shiraz, H. Improvement of microstrip patch antenna gain and bandwidth at 60 GHz and X bands for wireless applications. IET Microwaves, Antennas & Propagation, 10(11):1167-1173, 2016.

21. Alkhamis, R., Wigle, J. and Song, H. Global positioning system and distress signal frequency wrist wearable dual-band antenna. *Microwave and Optical Technology Letters*, 59(8):2057-2064, 2017.

22. Song, L. and Rahmat-Samii, Y. A systematic investigation of rectangular patch antenna bending effects for wearable applications. *IEEE Transactions on Antennas and Propagation*, 66(5):2219-2228, 2018.